




# Characterisation of size distribution and positional misalignment of nanoscale islands by small-angle X-ray scattering

Cite as: J. Appl. Phys. 125, 014301 (2019); <https://doi.org/10.1063/1.5050882>

Submitted: 03 August 2018 . Accepted: 06 December 2018 . Published Online: 02 January 2019

Georg Heldt, Philip Thompson , Rajesh V. Chopdekar , Joachim Kohlbrecher, Stephen Lee, Laura J. Heyderman , and Thomas Thomson 



View Online



Export Citation



CrossMark

## ARTICLES YOU MAY BE INTERESTED IN

[Phonon properties and thermal conductivity from first principles, lattice dynamics, and the Boltzmann transport equation](#)

Journal of Applied Physics **125**, 011101 (2019); <https://doi.org/10.1063/1.5064602>

[High-pressure neutron diffraction study of Pd<sub>3</sub>Fe](#)

Journal of Applied Physics **125**, 015901 (2019); <https://doi.org/10.1063/1.5079804>

[Perspective: Nanoscopy of charge kinetics via terahertz fluctuation](#)

Journal of Applied Physics **125**, 010901 (2019); <https://doi.org/10.1063/1.5079534>

## Ultra High Performance SDD Detectors



See all our XRF Solutions

# Characterisation of size distribution and positional misalignment of nanoscale islands by small-angle X-ray scattering

Cite as: J. Appl. Phys. **125**, 014301 (2019); doi: [10.1063/1.5050882](https://doi.org/10.1063/1.5050882)

Submitted: 3 August 2018 · Accepted: 6 December 2018 ·

Published Online: 2 January 2019



Georg Heldt,<sup>1,2</sup> Philip Thompson,<sup>1</sup>  Rajesh V. Chopdekar,<sup>2</sup>  Joachim Kohlbrecher,<sup>2</sup> Stephen Lee,<sup>3</sup> Laura J. Heyderman,<sup>2,4</sup>  and Thomas Thomson<sup>1</sup> 

## AFFILIATIONS

<sup>1</sup>School of Computer Science, University of Manchester, Manchester M13 9PL, United Kingdom

<sup>2</sup>Paul Scherrer Institut (PSI), 5232 Villigen, Switzerland

<sup>3</sup>School of Physics and Astronomy, University of St Andrews, North Haugh, St Andrews KY16 9SS, United Kingdom

<sup>4</sup>Laboratory for Mesoscopic Systems, Department of Materials, ETH Zurich, 8093 Zurich, Switzerland

## ABSTRACT

Highly ordered arrays of nanoscale magnetic structures form the basis of artificial spin ices, uniform particles for bio-medical applications, and data storage as Bit Patterned Media. We demonstrate that small-angle X-ray scattering (SAXS) allows the size distribution and the positional alignment of highly ordered arrays to be determined with high spatial and statistical accuracy. The results obtained from the SAXS measurements are compared to an analysis of Scanning Electron Microscopy images and found to be in excellent agreement. This confirms the validity of the technique and demonstrates its potential as a fast, accurate, and statistically reliable method for characterising arrays of ordered nanostructures.

© 2018 Author(s). All article content, except where otherwise noted, is licensed under a Creative Commons Attribution (CC BY) license (<http://creativecommons.org/licenses/by/4.0/>). <https://doi.org/10.1063/1.5050882>

## I. INTRODUCTION

Highly ordered arrays of nanostructures play a key role in many aspects of modern science and technology, such as in artificial spin ices,<sup>1,2</sup> as resonant enhancers in plasmonics,<sup>3,4</sup> in magnetic data storage drives as Bit Patterned Media (BPM),<sup>5-7</sup> for functionalisation of material surfaces,<sup>8</sup> and in biomedical science studying proteins.<sup>9</sup> In general, the fabrication of such arrays involves several process steps that inevitably lead to a certain distribution of structural parameters. To take full advantage of the desired properties of ordered arrays of nanostructures, it is essential to know the structural parameters including mean diameter, standard deviation of the diameter, and position misalignment. These parameters can be used to optimise the fabrication process<sup>10</sup> or in theoretical calculations and simulations to predict the performance of the array, for example, in BPM<sup>5-7</sup> or artificial spin ices.<sup>11,12</sup>

Real space imaging techniques used to characterise nanostructure arrays such as Atomic Force Microscopy (AFM)<sup>13</sup> or Scanning Electron Microscopy (SEM)<sup>14</sup> are usually

limited in the number of islands that can be measured in a single image as these are serial methods where the sample is scanned, resulting in appreciable measurement times. Consequently, the statistical significance of these experiments is often difficult to obtain, especially in applications where large numbers of nanoislands ( $\gg 10^5$ ) are involved. Small-angle X-ray scattering (SAXS) measurements offer the possibility to investigate a very large number of nanoislands simultaneously in parallel, reducing measurement times to the order of seconds. This provides a method of characterising large arrays of highly ordered nearly uniform nanoislands with high statistical significance. In order to evaluate the capabilities of SAXS to characterise arrays of nanomagnetic islands, we measured a systematic series of samples. The principal variable was the periodicity of the islands which was varied between 50 nm and 250 nm. The individual island diameter ranged between 15 nm and 40 nm with the largest islands corresponding to the arrays of greatest period. This resulted in arrays with diameter/pitch ratios varying

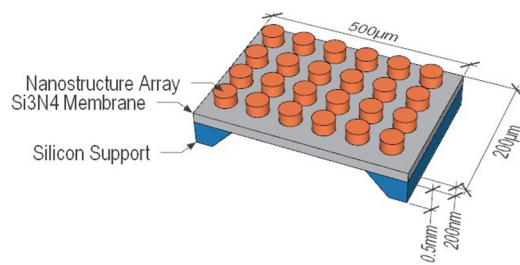


**FIG. 1.** Schematic of the SAXS sample showing the underlying silicon support and the  $\text{Si}_3\text{N}_4$  membrane, which is X-ray transparent.

between 0.16 and 0.3, which covers a significant part of the range of ratios encountered in the literature.<sup>5–7</sup>

## II. EXPERIMENTAL

In this work, we report on SAXS experiments using synchrotron radiation undertaken on large arrays of highly ordered, nearly uniform nanoislands ( $10^6$ – $10^8$  islands). The measured scattering data are analyzed using a modified scattering equation to determine the island size distribution and position misalignment. The results obtained were compared to SEM measurements of the same nanoislands to validate the SAXS data.

The samples investigated consisted of arrays of magnetic islands fabricated on X-ray transparent  $\text{Si}_3\text{N}_4$  membranes using a lift-off process. A bilayer (950 K/50 K) polymethylmethacrylate (PMMA) resist was employed to ensure well-defined island edges and to create a negative sidewall profile. The resist was spin-coated onto a Si supported  $\text{Si}_3\text{N}_4$  membrane and then exposed using an electron beam writer (Vistec EBPG 5000+). Following the development of the resist, a magnetic thin film of Ta (2)/Pd (3)/[Co (0.3)/Pd (0.9)]<sub>8</sub>/Pd (1.1), where all thicknesses are in nm and the total thickness is 15.7 nm, was deposited on the patterned resist by DC magnetron sputtering. Finally, the remaining resist was lifted off and the supportive Si was removed by wet etching in potassium hydroxide (KOH) solution, creating

a sample with an X-ray transparent region of  $500 \times 200 \mu\text{m}^2$ . The island diameter ( $\leq 40$  nm) was designed to create a series of arrays where the diameter/period ratio was between 0.16 and 0.30. A systematic series of square lattice arrays were designed with periodicities of 50, 60, 70, 80, 100, and 250 nm (Fig. 1).

The SAXS characterisation was conducted at the coherent Small-Angle X-ray Scattering beamline X12SA at the Swiss Light Source with an X-ray energy of 7.71 keV, close to the K-edge absorption of the Co nanoislands demonstrating the potential of extending the technique to resonant X-ray scattering.<sup>15</sup> The energy resolution was  $\frac{\Delta E}{E} < 0.02\%$  and the photon flux at the sample position was approximately  $10^{12}$  photons/s. The measurements were performed with the X-ray beam at normal incidence with respect to the patterned sample surface and an illumination area of approximately  $50 \mu\text{m}$  diameter. The SAXS measurements presented here are sensitive to structural dimensions of  $\approx 5$ –100 nm with the lower limit being approached for the small-period nanostructure arrays. The X-ray exposure for a single measurement takes only a few seconds. The scattering patterns were detected with a 2D Pilatus detector ( $1475 \times 1679$  pixels, pixel size  $172 \times 172 \mu\text{m}^2$ ). A 7 m evacuated drift tube was placed in the beam path between the sample and the detector to minimise air scattering. The measured area was subdivided into a  $3 \times 3$  matrix giving 9 squares of equal size across the surface. Measurements on each of these square areas were repeated 6 times for 2 s. This procedure reduces measurement artefacts and keeps the heat load to a minimum, thus avoiding distortions. Alignment and averaging of each measurement area was performed to produce a single data set for analysis.

## III. DATA REDUCTION OF SAXS MEASUREMENT

An example SAXS measurement performed on the 250 nm period nanoisland array is given in Fig. 2(a), showing the scattering intensity  $I(x,y)$ . The position vectors  $x$  and  $y$  correspond to the pixels on the 2D detector, and the scattering amplitude (using a Log scale) is represented by the height and colour of pixel. Due to the long-range periodicity of the nanoisland locations in real space, the resulting diffraction pattern

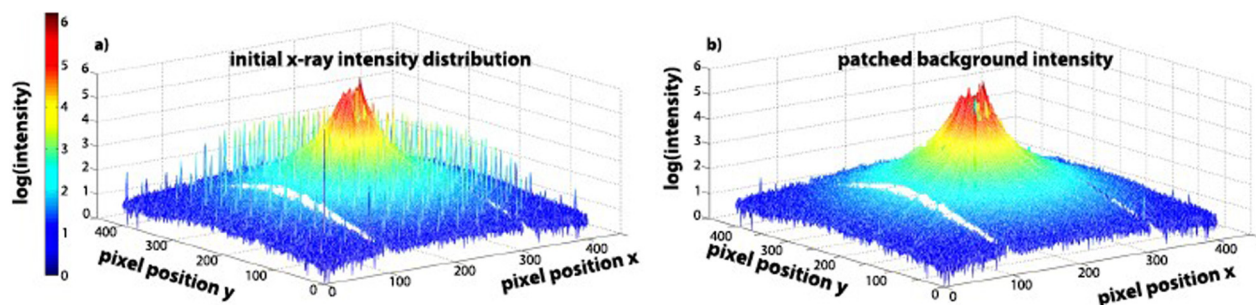


**FIG. 2.** Measured (a) X-ray intensity distribution for the 250 nm period nanoisland array and (b) the corresponding background intensity using a patch method algorithm to produce a complete background.

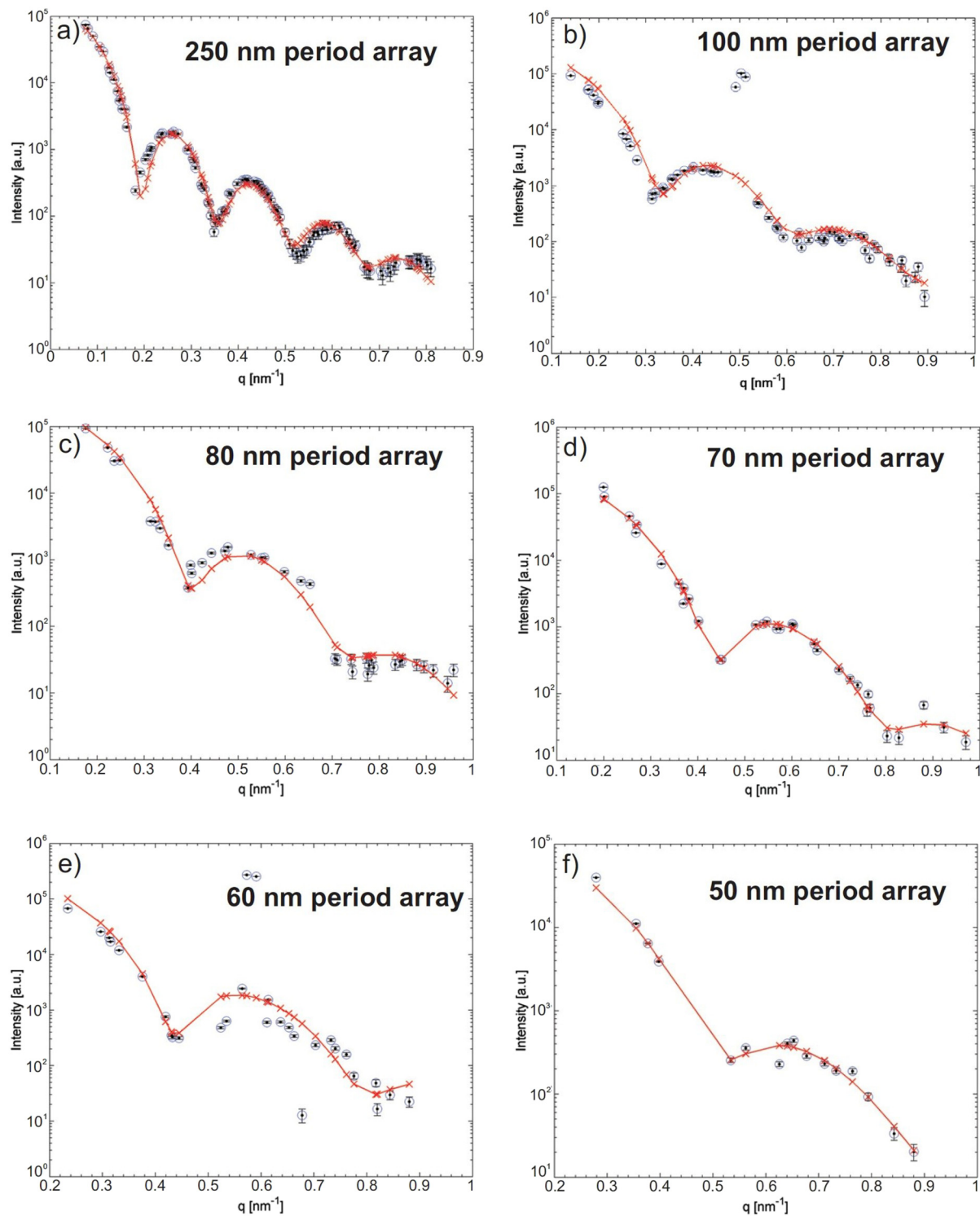


**FIG. 3.** Measured intensity distribution (black circles) and model fits (red crosses joined by lines) for nanostructure arrays with periods 250, 100, 80, 70, 60, and 50 nm. Note, the x-axis is scaled to show the  $q$ -range of interest for each array period.

contains several thousand individual “Bragg peaks” similar to those arising from scattering by crystals of atoms in large angle-diffraction. As in diffraction from atomic crystals, in our 2D arrays of nanostructures, the amplitude of these peaks in reciprocal space is modulated due to the finite size of the nanoislands in real space *via* the Fourier transform of the cylindrical shape of the islands (see Sec. IV). This is analogous to the modulation of diffraction peaks by the atomic form factor in large-angle diffraction. We note that, in principle, different form factors could be used to model a range of geometries. The nodes in this function lead to circular nodes around the beam centre in the intensity of diffraction peak heights, as visible toward the edge of the pattern in Fig. 2(a), where the intensity of the peaks is significantly reduced. In addition to these nodes, the form factor also leads to an overall rapid reduction in diffraction amplitude as a function of reciprocal wavevector  $q$ . There is an additional source of intensity reduction with  $q$  due to the random positional disorder of individual scatters about their ideal positions on the real space lattice. By analogy with the Debye-Waller factor in atomic scattering, this can be modeled by a term  $G(q) = \exp(-Bq^2)$ , where  $B$  is a constant and  $q = 4\pi \sin(\theta)/\lambda$ .<sup>16,17</sup> We define the scattering angle,  $(\theta/2)$ , as the angle between the incident and scattered beam with  $\lambda$  as the wavelength of the beam. The combined effects lead to intensity variations of over five orders of magnitude in some of our data. The scattering pattern in reciprocal space thus contains information about both the perfection of the real-space lattice and the size, shape, and dispersity of the nanoislands in real space.

Prior to fitting the measured diffraction intensities, any background signal must be removed including the contribution from the direct beam. To obtain an estimate for the background signal, we employ a so-called “patch” method of background subtraction. With the patch method, the data from an area of the two-dimensional detector ( $x, y$ ) where a diffraction peak is located are removed. An algorithm identifies each diffraction peak as they are standalone points with values much higher than the background intensity. These points are then subtracted from the intensity measurement, leaving only the background intensity and gaps in the data from where the diffraction peaks have been removed. To compensate for these gaps, a running average is applied, which takes the gradient of the surrounding area and applies it to the gap. Thus, the intensity is smoothed to produce a continuous background intensity [Fig. 2(b)]. To obtain the diffraction data, the total background intensity, shown in Fig. 2(b), is subtracted from the X-ray intensity distribution [Fig. 2(a)]. The background-subtracted data, which consist of the diffraction peaks modulated by the form factor, are used for all subsequent analyses.

With decreasing array periodicity, additional low-intensity peaks appear in the vicinity of the expected diffraction-peaks corresponding to the array pitch. These “satellite peaks” have an intensity of one or two orders of magnitude lower than the expected diffraction-peak. Therefore, the satellite peaks are easily identifiable and can be removed from the diffraction data; thus, only the expected diffraction-peaks are fitted.

Satellite peaks arise due to small imperfections in the periodicity of the array. These imperfections are typically very difficult to quantify using direct imaging techniques due to the simultaneous requirement of high measurement accuracy and a large field of view. In these samples, satellite peaks most likely arise from the electron-beam lithography process where the array is not written continuously but rather in fields, with the size of the main field of the order of  $100\ \mu\text{m}$  and the size of the subfields of the order of  $1\ \mu\text{m}$ . It is likely that the stitch error between different write fields causes a relative shift or tilt between the various nanostructured fields, so giving rise to the satellite peaks. While the analysis of such satellite peaks can give insight into subtle larger-scale misalignment of the array elements, rejection of these satellite peaks does not influence the modeling of the island form factor described in Sec. IV.

#### IV. THEORY AND ANALYSIS OF SAXS DATA

Due to the square symmetry of the lattice, many symmetrically equivalent peaks in the diffraction pattern lie at the same  $q = |\mathbf{q}|$  from the centre of reciprocal space and hence at the same distance from the beam centre in the 2D diffraction pattern. Each diffraction peak is spread over a number of pixels, so the integrated intensity can be obtained reliably. To explore the  $q$ -dependence of the peaks, the intensities of all equivalent peaks can be averaged and folded onto a 1D axis, making appropriate corrections for the multiplicity of

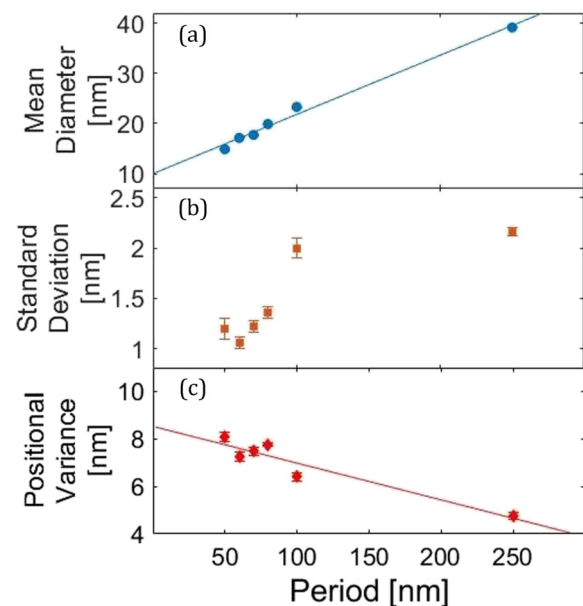


**FIG. 4.** Plot of the mean diameter obtained from fitting and averaging all the SAXS measurements for each sample in the periodicity series. The uncertainty in (a) the mean diameter is within the symbol. In (b), the standard deviation is an indication of the polydispersity of island diameters, and in (c), the positional variance is the variation in island position relative to the ideal square lattice. The data are tabulated in the [supplementary material](#).

each peak. As a beam stop was used to protect the detector, the beam centre was determined by fitting a 2D Gaussian function to the background data, shown in Fig. 2(b), from which the position of maximum intensity was calculated. The distance in pixel numbers from the beam centre (Fig. 2) is converted to scattering vector  $q$  using the known geometric parameters. The experimental setup included a drift tube of length 7.0885 m, which permitted scattering vectors up to  $q \approx 0.96 \text{ nm}^{-1}$  to be measured. The gaps in measured intensity (white lines in Fig. 2) are due to joins in the 2D detector array. These joins do not affect the analysis as any peaks that would have occurred within these white lines do not contribute to the average peak intensity for that set. The affected regions are small, and thus their contribution, which would lower the signal-to-noise ratio, is not significant and the mean value for the intensity is not adversely affected.

The reduced and calibrated data were analyzed using a Matlab program. The starting point for the analysis of the coherent scattering is the generalised scattering intensity equation for an ensemble of identical scattering objects<sup>18–21</sup>

$$I(q) = I_0(b_1 - b_2)^2 \frac{N}{V} [F^2(qR)G(q) S(q)]. \quad (1)$$

The first three terms (incident beam intensity  $I_0$ , object scattering length density difference  $(b_1 - b_2)$  between the scatterers and the matrix, and the number density  $\frac{N}{V}$ ) can be condensed into one parameter since these terms are independent of the scattering vector  $q$  and are constant. In our case, the nanoislands are surrounded by vacuum, so the combined term is simply a scattering length density for the nanoislands. During the experiment, the measured intensities are corrected using a beam monitor to ensure an effective constant flux for the

reduced data, although the absolute intensity is not necessary for the analysis as we fit a normalised function to the data. The so-called form factor  $F(qR)$  is the Fourier transform of the shape of the sample, that is of a cylinder of radius  $R$ .<sup>22–25</sup> In typical small-angle scattering, the term  $S(q)$  reflects the Fourier transform of the spatial arrangement of the scatterers in real space. Since our real space lattice consists of a periodic square array of objects, this is simply a delta function  $S(\mathbf{q}) = \delta(\mathbf{q} - \mathbf{K})$ , where  $\mathbf{K}$  are reciprocal lattice points, that is, we have diffraction peaks. As discussed above,  $G(q)$  is an effective Debye-Waller factor.<sup>18,19,21</sup> We thus effectively fit the normalised function

$$I_N(q) = [F^2(qR)G(q)] \quad (2)$$

to the integrated intensities at the points  $q = |\mathbf{K}|$ .

To fit the measured intensity distribution accurately, Eq. (2) must be modified to account for polydispersity in the form factor, which captures the variation in diameter of the islands,

$$I_{\text{tot}}(q) = \int p(R)F^2(q, R)dR G(q), \quad (3)$$

where the Debye-Waller factor is explicitly given by

$$G(q) = \exp(-q^2 \sigma_{\text{pos}}^2). \quad (4)$$

The diameter distribution is modeled as a Gaussian function, which is used as a weighting function for the form factor, given as

$$p(R) = \frac{\exp\left[-\frac{1}{2}\left(\frac{R-\mu}{\sigma}\right)^2\right]}{\sigma\sqrt{2\pi}}. \quad (5)$$

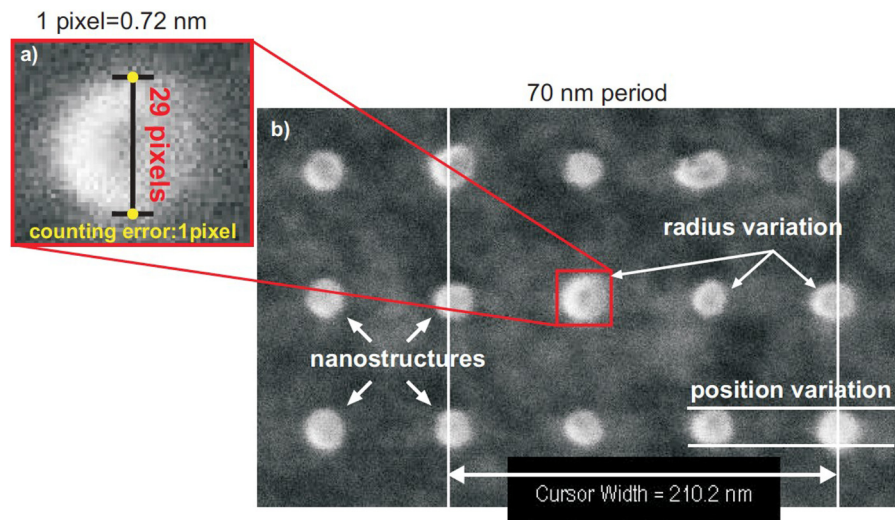


**FIG. 5.** SEM image of a nanostructure array demonstrating the determination of the nanostructure diameter by pixel counting (a). The counting error at the edge, both top and bottom, of the structure was estimated with 1 pixel shown by the yellow circles. Additionally, in image (b), two structural variations, in the position and diameter of the nanostructures, are observed which can be quantified by Eq. (7).

The form factor can be factorised as both parallel and perpendicular alignment to the sample surface. Therefore, the form factor has the following form:

$$F^2(q, R, L, \theta) = (\pi R^2 L)^2 \left( \frac{\sin[q \cos(\theta) \frac{L}{2}]}{q \cos(\theta) \frac{L}{2}} \cdot \frac{2J_1[qR \sin(\theta)]}{qR \sin(\theta)} \right)^2 \quad (6)$$

For the experimental geometry used here,  $\theta = 90^\circ$ . Therefore, under normal X-ray incidence parallel to the cylinder axis, the form factor simplifies to

$$F^2(q, R) = (\pi R^2 L)^2 \left( \frac{2J_1(qR)}{qR} \right)^2 \quad (7)$$

The total scattering intensity used for fitting the diffraction

data is thus<sup>18,25</sup>

$$I_{\text{tot}}(q) = \int \frac{\exp\left[-\frac{1}{2}\left(\frac{R-\mu}{\sigma}\right)^2\right]}{\sigma\sqrt{2\pi}} (\pi R^2 L)^2 \left(\frac{2J_1(qR)}{qR}\right)^2 dR \exp(-q^2\sigma_{\text{pos}}^2), \quad (8)$$

where  $L$  and  $R$  are the length (equivalent to the thickness of the film) and radius of the cylinder, respectively, and  $J_1$  is a Bessel-function of the first kind. Fitting Eq. (8) to the measured data allows values for the mean radius (diameter), standard deviation, and positional variance to be determined.

## V. RESULTS

The integrated SAXS diffraction data (symbols) are shown in Figs. 3(a)–3(f) where the intensity of the scattering is

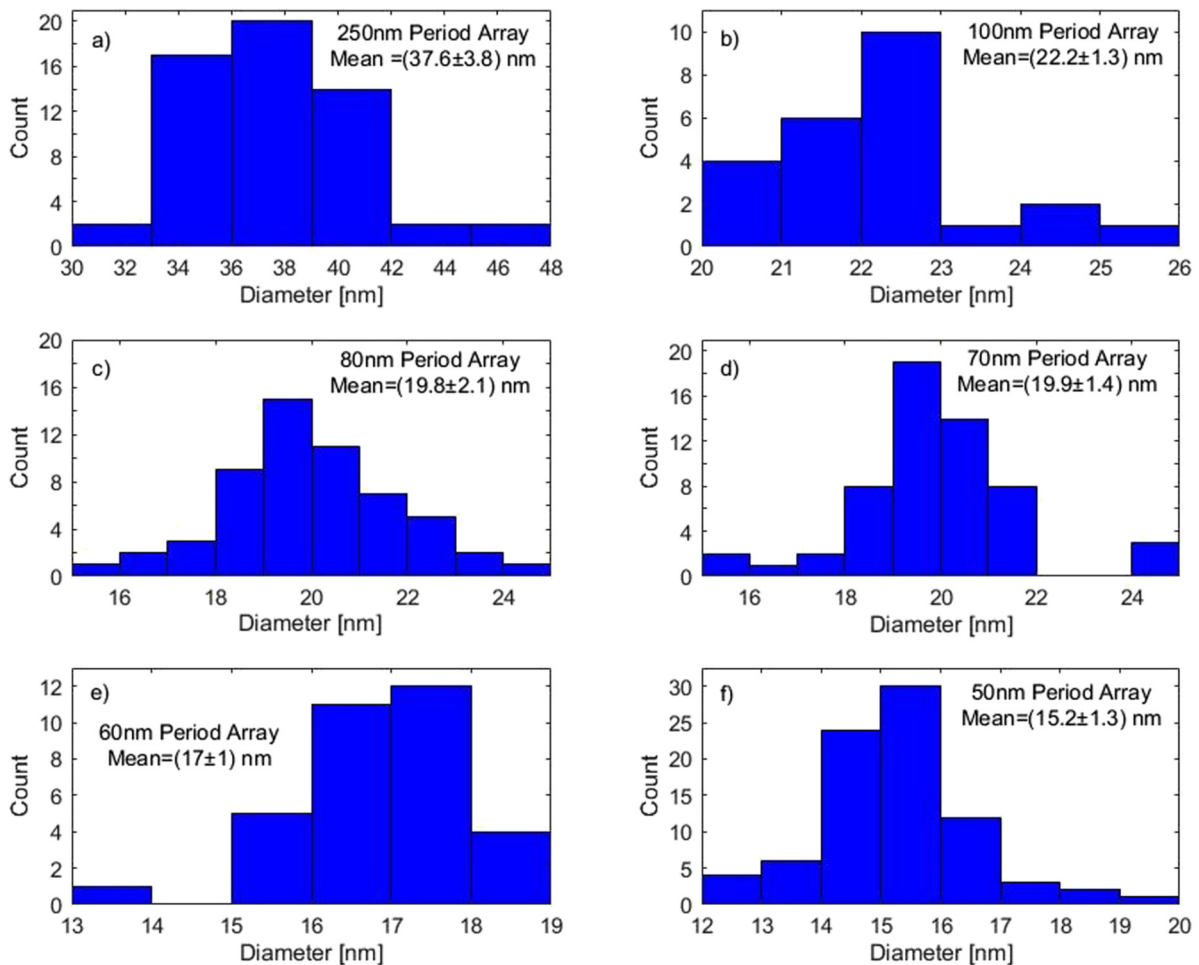


FIG. 6. (a)–(f) Histograms of island diameters obtained from a manual analysis of multiple SEM images of highly ordered arrays of nanoscale magnetic structures where the array period was varied between 250 nm and 50 nm. The error was assumed to be  $\pm 2$  pixels.

plotted against scattering vector  $q$ . The data include error bars, but these are only visible within the symbols at low intensities. The solid lines are the fits to the data obtained using the model and procedures described in Sec. IV. The quality of fit for each position was assessed by the degrees of freedom corrected  $r^2$ -value (Adjusted R square) and the root mean square error (RMSE). As the measured area is subdivided into 9 squares, the quality of the fit for each square is reflected in the uncertainty of the fit parameters. To obtain averaged structural parameters for the array, the uncertainty of each set of 9 parameters was considered and the mean value for the array was obtained by weighting the contributions of the individual squares by the uncertainty in the fit. The values for uncertainties obtained from the fits were found to be  $>0.9$  for Adjusted R squared and between 0.2 and 0.4 for the root mean square error.

Fitting the model to the data provides values for the mean diameter, standard deviation of the diameter, and positional variance. The fit also provides an estimate of the uncertainty in the values for each of these parameters. In Fig. 4, results are shown for island diameter, standard deviation of the island diameter, and positional variance for the series of island arrays measured. The Gaussian distributions modeled from the polydispersity of island diameters determined from these parameters are provided in the [supplementary material](#). The diffraction data show that the diameter is, to a close approximation, a linear function of the period for the lithography process employed and are consistent with the parameters expected, where for large centre-to-centre distances, the mean diameter is greater than for smaller centre-to-centre distances.

It can also be seen that the positional variance of the island arrays is a significant fraction of the island diameter as the period and diameter decrease. This information demonstrates the effectiveness of SAXS as a measurement technique to provide information that can be used to optimise fabrication methods in order to create near perfect island arrays over large areas. These data can also be used directly to predict the performance of samples fabricated using the current process, for example, as BPM.<sup>26–28</sup>

Having demonstrated the feasibility of SAXS as a technique to characterise nanoscale islands with high statistical precision, we now verify the accuracy of the measurements with real-space SEM imaging. A Carl-Zeiss Supra VP55 SEM using an accelerated voltage of 7 kV with a resolution of 0.7 nm was employed. The SEM technique is a well-established laboratory based imaging technique with sub-nanometre spatial resolution. To obtain statistically meaningful measurements of the distribution of island diameters, multiple images must be analyzed, as the field of view limits the number of islands visible per image. The analysis of these images was performed by counting each pixel by hand that, although quite time consuming, provides an accurate measurement of size. The data obtained from this measurement found the diameter and distribution within an error of 2 pixels. We note that in future, the growing availability of sophisticated image processing software, possibly incorporating Artificial

Intelligence, will likely further improve the analysis time and accuracy of the results obtained from direct imaging techniques.

An example SEM image is shown in Fig. 5 where the individual pixels are counted and then converted into a measurement of the diameter. Here, measurements of orthogonal diameters are recorded and averaged for each nanostructure. Conversion uses pixel count and, therefore, the number of possible pixels limits the accuracy of this method. Conversion used 1 pixel = 0.72 nm, given by the calibrated magnification used during the measurement.

The results for SEM measurements are plotted as histograms and shown in Figs. 6(a)–6(f), where the values measured are the diameter of the nanostructures.

In order to understand how the measurements compare with SAXS diffraction data, the parameters obtained from both methods are compared in Fig. 7.

It can be seen from the data in Fig. 7 that the two methods produce, within error, identical results. The uncertainties associated with the SEM measurement are considerably greater reflecting the poorer counting statistics inherent in the methodology. The correlation obtained between the two methods demonstrates the utility of the SAXS technique. SAXS produces reliable, accurate results with much higher statistical confidence due to the large area measured in parallel,  $500\ \mu\text{m} \times 200\ \mu\text{m}$  for SAXS compared with  $2.1\ \mu\text{m} \times 2.1\ \mu\text{m}$  for SEM, and at a fraction of the time needed in comparison to the SEM measurement and analysis.

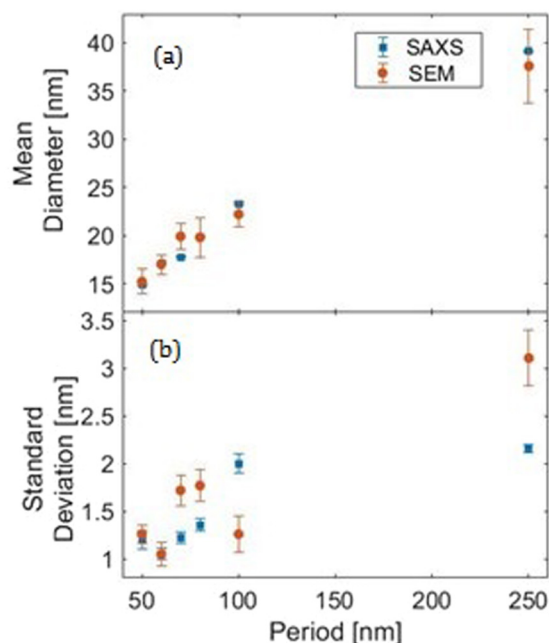


FIG. 7. Comparison of (a) the mean diameter and (b) standard deviation of the nanoislands obtained from SEM and SAXS measurements.



## VI. CONCLUSION

We have demonstrated that values for mean diameter, standard deviation, and positional variance are measurable using the SAXS method for nanostructure arrays. The validity of this experiment was tested by comparing SAXS results with SEM data, which is a well-established technique for imaging nanostructures. The data demonstrate that values obtained using the two techniques are identical within error. The statistical significance of the SAXS diffraction data is considerably better since orders of magnitude more islands may be sampled in a measurement time of seconds. Therefore, the SAXS method is a valid alternative to SEM and other imaging techniques for measuring nanostructure arrays producing data with much greater statistical significance and much reduced measurement time. Indeed, the increasing capabilities of laboratory-based instruments should allow SAXS measurements to be utilised routinely rather than using synchrotron source employed. It also offers the possibility of probing small imperfections in highly ordered arrays through an analysis of satellite peaks. Although we focused our measurements on cylindrical nanostructures, it is possible to measure a variety of nominally identical nanostructure arrays with translational symmetry using this method where the shape of the structures does not limit its accuracy.

## SUPPLEMENTARY MATERIAL

A normalised probability distribution for SAXS measurements, as well as values for Figs. 4 and 7, can be found in the [supplementary material](#).

## ACKNOWLEDGMENTS

The authors gratefully acknowledge the contribution of the Engineering and Physical Sciences Research Council (EPSRC) (Grant No. EP/G032440/1) toward funding this work.

## REFERENCES

- <sup>1</sup>L. J. Heyderman and R. L. Stamps, "Artificial ferroic systems: Novel functionality from structure, interactions and dynamics," *J. Phys.* **25**, 363201 (2013).
- <sup>2</sup>C. Nisoli, R. Moessner, and P. Schiffer, "Colloquium: Artificial spin ice: Designing and imaging magnetic frustration," *Rev. Modern Phys.* **85**(4), 1473–1490 (2013).
- <sup>3</sup>L. Zhao, K. L. Kelly, and G. C. Schatz, "The extinction spectra of silver nanoparticle arrays: Influence of array structure on plasmon resonance wavelength and width," *J. Phys. Chem. B* **107**(30), 7343–7350 (2003).
- <sup>4</sup>B. Lamprecht, G. Schider, R. Lechner, H. Ditlbacher, J. Krenn, A. Leitner, and F. Aussenegg, "Metal nanoparticle gratings: Influence of dipolar particle interaction on the plasmon resonance," *Phys. Rev. Lett.* **84**(20), 4721–4724 (2000).
- <sup>5</sup>P. W. Nutter, Y. Shi, B. D. Belle, and J. J. Miles, "Understanding sources of errors in bit-patterned media to improve read channel performance," *IEEE Trans. Magn.* **44**(11), 3797–3800 (2008).
- <sup>6</sup>H. J. Richter, A. Y. Dobin, O. Heinonen, K. Z. Gao, R. J. M. V. D. Verdonk, R. T. Lynch, J. Xue, D. Weller, M. F. Erden, and R. M. Brockie, "Recording on bit-patterned media at densities of 1Tb/in<sup>2</sup> and beyond," *IEEE Trans. Magn.* **42**(10), 2255–2260 (2006).
- <sup>7</sup>Y. Shi, P. W. Nutter, B. D. Belle, and J. J. Miles, "Error events due to island size variations in bit patterned media," *IEEE Trans. Magn.* **46**(6), 1755–1758 (2010).
- <sup>8</sup>M. Li, H. Schnablegger, and S. Mann, "Coupled synthesis and self-assembly of nanoparticles to give structures with controlled organization," *Nature* **402**, 393–395 (1999).
- <sup>9</sup>V. Uversky, "Natively unfolded proteins: A point where biology waits for physics," *Protein Sci.* **11**(4), 739–756 (2002).
- <sup>10</sup>H. Nalwa, *Handbook of Thin Film Materials* (Academic Press, Boston, 2002).
- <sup>11</sup>A. Farhan, P. Derlet, A. Kleibert, A. Balan, R. Chopdekar, M. Wyss, J. Perron, A. Scholl, F. Nolting, and L. Heyderman, "Direct observation of thermal relaxation in artificial spin ice," *Phys. Rev. Lett.* **111**(5), 057204 (2013).
- <sup>12</sup>E. Mengotti, L. Heyderman, A. Rodríguez, F. Nolting, R. Hügli, and H. Braun, "Real-space observation of emergent magnetic monopoles and associated Dirac strings in artificial kagome spin ice," *Nature Phys.* **7**(1), 68–74 (2010).
- <sup>13</sup>E. A. Dobisz, S. L. Brandow, R. Bass, and L. M. Shirey, "Nanolithography in polymethylmethacrylate: An atomic force microscope study," *J. Vac. Sci. Technol. B* **16**, 3695–3700 (1998).
- <sup>14</sup>L. Alink, J. P. J. Groenland, J. de Vries, and L. Abelmann, "Determination of bit patterned media noise based on island perimeter fluctuations," *IEEE Trans. Magn.* **48**(11), 4574–4577 (2012).
- <sup>15</sup>B. Ravel, Cobalt foil measured at nsls x11b November 2003 by Bruce Ravel, xas standard reference material (2003), see <http://cars9.uchicago.edu/ravel/software/doc/-Standards/co.html>.
- <sup>16</sup>P. Debye, "Interferenz von Röntgenstrahlen und Wärmebewegung," *Annalen der Physik* **348**(1), 49–92 (1913).
- <sup>17</sup>I. Waller, "Zur Frage der Einwirkung der Wärmebewegung auf die Interferenz von Röntgenstrahlen," *Zeitschrift für Physik* **17**(1), 398–408 (1923).
- <sup>18</sup>R. W. Richards and J. L. Thomason, "Simulation of small-angle neutron scattering from microphase-separated block copolymers," *Macromolecules* **18**(3), 452–460 (1985).
- <sup>19</sup>B. L. Brown and T. Taylor, "A computer simulation study of the low-angle X-ray scattering obtained from triblock copolymers," *J. Appl. Polymer Sci.* **18**(5), 1385–1396 (1974).
- <sup>20</sup>O. Kratky and G. Porod, "Diffuse small-angle scattering of X-rays in colloid systems," *J. Colloid Sci.* **4**(1), 35–70 (1949).
- <sup>21</sup>S. Förster, S. Fischer, K. Zielske, C. Schellbach, M. Sztucki, P. Lindner, and J. Perlich, "Calculation of scattering-patterns of ordered nano- and meso-scale materials," *Adv. Colloid Interface Sci.* **163**(1), 53–83 (2011).
- <sup>22</sup>O. Glatter and O. Kratky, *Small Angle X-Ray Scattering* (Academic Press, London, 1982).
- <sup>23</sup>A. Guinier and G. Fournet, *Small Angle X-Ray Scattering of X-Rays* (John Wiley and Sons, New York, 1955).
- <sup>24</sup>B. Korgel, S. Fullam, S. Connolly, and D. Fitzmaurice, "Assembly and self-organization of silver nanocrystal superlattices: Ordered 'soft spheres'," *J. Phys. Chem. B* **102**(43), 8379–8388 (1998).
- <sup>25</sup>C. Murray, C. Kagan, and M. Bawendi, "Synthesis and characterization of monodisperse nanocrystals and close-packed nanocrystal assemblies," *Annu. Rev. Mater. Sci.* **30**(1), 545 (2000).
- <sup>26</sup>J. Kalezhi, S. J. Greaves, Y. Kanai, M. E. Schabes, M. Grobis, and J. J. Miles, "A statistical model of write-errors in bit patterned media," *J. Appl. Phys.* **111**, 053926 (2012).
- <sup>27</sup>Y. Shi, P. Nutter, and J. Miles, "Performance evaluation of bit patterned media channels with island size variations," *IEEE Trans. Commun.* **61**(1), 228–236 (2013).
- <sup>28</sup>Y. Wang and B. V. K. Vijaya Kumar, "Write modeling and read signal processing for heat assisted bit-patterned media recording," *IEEE Trans. Magn.* **54**, 3000510 (2018).